Q. J. R. Meteorol. Soc. (2004), **130**, pp. 1723–1748 doi: 10.1256/qj.03.63

Inversion effects on mountain lee waves

By S. B. VOSPER*
Met Office, Exeter, UK

(Submitted 7 April 2003; revised 20 November 2003)

SUMMARY

The effect of a sharp low-level temperature inversion on flow over a mountain is investigated via a series of two-dimensional idealized numerical model simulations. The main focus of the study is the effect of the inversion on the formation of lee waves, lee-wave rotors, low-level hydraulic jumps and the occurrence of wave breaking aloft. The idealized problem considered consists of an upwind velocity profile that is independent of height (above the boundary layer) and directed normal to an isolated two-dimensional ridge. The upstream stratification consists of a neutral layer immediately above the ground capped by a sharp temperature inversion. Above this, the atmosphere is stably stratified and the Brunt–Väisälä frequency is independent of height. Simulations were conducted for a range of inversion strengths (measured by the difference in potential temperature across the inversion) and inversion heights. The effect of both a free-slip and a no-slip lower boundary condition is investigated. Results show that, when the upwind Froude number (defined in the usual way for two-layer shallow-water flow) falls below a critical value, a short-wavelength resonant lee wave forms downwind of the mountain on the inversion. It is shown that both the critical Froude-number value and the wavelength of the lee wave are accurately predicted by linear theory. The lee-wave amplitude, however, can be significantly underestimated by linear theory if the wavelength is less than the hill length scale. In the case of a no-slip boundary condition, if the wave amplitude is sufficiently large, boundary-layer separation occurs underneath the wave crests and closed rotor circulations occur. In general, flow separation (and rotors) do not occur in the free-slip case. In both the free-slip and no-slip flows, as the Froude number decreases the lee wave is eventually replaced by a stationary hydraulic jump above the lee slope of the mountain.

KEYWORDS: Hydraulic jump Rotor Temperature inversion Trapped lee wave

1. INTRODUCTION

Forecasting the occurrence of severe low-level turbulence over mountainous terrain is a very challenging, yet important, aspect of weather prediction. Accurate forecasts of downslope wind storms or lee-wave rotors, for example, could help improve aviation safety and would be of general benefit to populations in mountainous regions. Although the trend towards finer resolution in operational numerical weather prediction (NWP) models means that some of the larger-scale effects of orography (e.g. wave drag) are now starting to be resolved, many of the small-scale details remain poorly represented. Since very-fine resolution ($\sim$1 km) NWP is currently only practical for limited areas, alternative methods, based for example on local knowledge of the flow behaviour, are necessary. Clearly these methods require a good understanding of orographic flows.

It has long been recognized that regions of recirculating airflow, or rotors, and zones of low-level turbulence are commonly occurring features of flow over mountains. Observational studies of rotors date back to the pioneering measurements made above the Alps (e.g. Kuettner 1939), the Sierra Nevada (e.g. Holmboe and Klieforth 1957) and more recent observations made by Ralph *et al.* (1997). A comprehensive review of these studies has been provided by Doyle and Durran (2002). It is only recently, however, that detailed numerical studies of the link between trapped lee waves and low-level turbulence have been conducted. Recent work by Doyle and Durran (2002) has highlighted the importance of lee waves in the formation of rotors. Through a series of numerical simulations, Doyle and Durran demonstrated that the existence of rotors depends crucially on the presence of friction at the ground. When the wave response is of sufficient amplitude, the wave-induced pressure gradient can lead to boundary-layer separation and regions of recirculation underneath the wave crests.

* Corresponding address: Met Office, FitzRoy Road, Exeter, Devon EX1 3PB, UK.
e-mail: simon.vosper@metoffice.com

In general, most theoretical studies of stratified flows over mountains have been restricted to idealized and simple upwind profiles of wind and stability that do not contain any fine-scale structure, such as that due to a sharp temperature inversion, for example. In the few studies in which sharp temperature inversions are represented, however, it appears that inversions can have a significant influence on the gravity-wave and near-surface flow structure. For example, in the linear theory developed by Klemp and Lilly (1975) (valid for hydrostatic mountain waves) the depth, height and temperature difference across the inversion play a crucial role in determining the strength of the downslope wind at the surface. Numerical simulations (e.g. Durran 1986; Wang and Lin 2000) also demonstrate the importance of inversions in the dynamics of gravity-wave breaking. There is, of course, a large body of literature on shallow-water flow over obstacles (see Baines (1995) for a comprehensive review) and, despite the absence of stable stratification (and hence energy propagation by internal gravity waves), the case of two-layer shallow-water flow is somewhat analogous to atmospheric flows with a sharp inversion. Indeed, as shown by Durran (1986), in nonlinear situations involving large-amplitude mountain waves the lee-slope flow is controlled by hydraulic theory to a good approximation.

Recent field observations (S. D. Mobbs, personal communication) made downwind of a mountain range on the Falkland Islands in the South Atlantic have demonstrated that a strong temperature inversion at the top of the boundary layer can contribute to severe low-level turbulence, the formation of rotors and strong downslope winds. Although its precise role is not clear, a sharp temperature inversion was also present in recent observations of a rotor cloud which formed downwind of an Arctic ice cap (Ozawa *et al.* 1998). It is also well known that a strong inversion capping the boundary layer can have a major impact on the flow in mountainous coastal regions. The strong subsidence inversion which occurs above the Californian coastal boundary layer (Dorman and Winant 1995), for example, is known to generate conditions favourable to flow blocking, expansion fans and hydraulic jumps (e.g. Ström *et al.* 2001). Colman and Dierking (1992) have also suggested that a strong inversion near the mountain top is one necessary condition for downslope windstorms encountered in south-east Alaska.

The purpose of this study is, through a series of idealized numerical simulations, to develop an understanding of how a sharp inversion can influence the gravity-wave dynamics and lead to rotor generation, hydraulic jumps and low-level wave breaking. To complement the simulations a linear theory is also developed. For simplicity we restrict attention to the situation where the atmosphere consists of two layers with different (constant) values of the Brunt–Väisälä frequency, N, and in which, in the absence of any mountain or boundary-layer effects, the wind speed, $\overline{U}$, is independent of height throughout the entire depth of the atmosphere. An inversion at the interface of the two layers is represented by a discontinuity, of magnitude $\Delta\overline{\theta}$, in the potential temperature, $\overline{\theta}(z)$. We shall suppose that the interface between the two layers occurs at a height z_{i} above the ground and that the stratification is neutral below z_{i}. This is a common situation in strong or moderate flows over hills since the boundary layer is often only weakly stable, or is neutral, below the inversion. A schematic diagram illustrating the two-layer atmosphere is shown in Fig. 1. For these idealized conditions, and for a hill with height H and width L, the dimensional scales can be combined to give four independent non-dimensional parameters which control the flow. These can be written as

$$F_{\mathrm{i}} = \frac{\overline{U}}{\sqrt{g' z_{\mathrm{i}}}}, \quad Z = \frac{N z_{\mathrm{i}}}{\overline{U}}, \quad F_L = \frac{\overline{U}}{NL} \quad \text{and} \quad S = \frac{H}{L}. \tag{1}$$

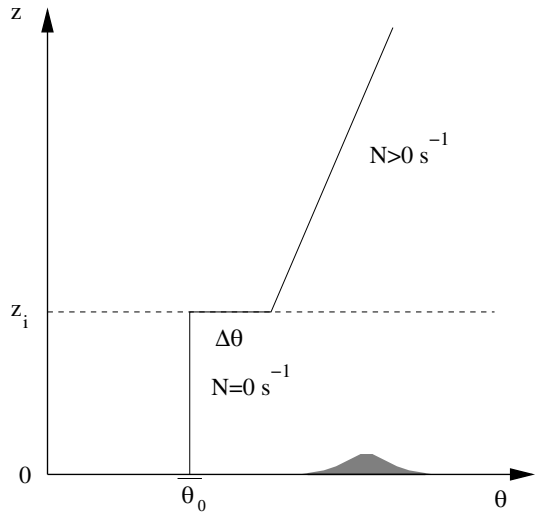

Figure 1. Schematic diagram illustrating the simple two-layer atmosphere. The inversion, characterized by a discontinuity of magnitude $\Delta\overline{\theta}$ in the potential temperature, occurs at a height $z = z_i$.

In the expression for F_i, g' is a reduced gravitational acceleration, given by $g' = g\Delta\overline{\theta}/\overline{\theta}_0$, g is the acceleration due to gravity and $\overline{\theta}_0$ is a reference potential temperature, here taken to be the value in the neutral layer. F_i is the Froude number of the flow and is the ratio of the flow speed to the speed of long-wavelength interfacial waves on the inversion in stationary fluid, when the stratification above is neutral (Baines 1995). The parameter Z is related to the ratio of inversion height to the vertical wavelength of hydrostatic mountain waves in the upper layer, S is a measure of the mountain slope and the parameter F_L is a measure of non-hydrostatic effects in the upper layer. For values of $F_L \ll 1$ the vertically propagating mountain-wave response will be hydrostatic to a good approximation. Note that, from combinations of the parameters in (1), two other important non-dimensional parameters can be defined which are useful in interpreting the flow characteristics. These are the non-dimensional mountain height, $NH/\overline{U}$, and the ratio of hill height to inversion height, H/z_i. In terms of the parameters in (1) these can be expressed as

$$\frac{NH}{\overline{U}} = SF_L^{-1} \quad \text{and} \quad \frac{H}{z_i} = SF_L^{-1}Z^{-1}. \tag{2}$$

It is worth noting here that both $\overline{U}/NH$ and F_L are also often referred to as Froude numbers in the literature. This has been discussed in some detail by Baines (1995) who argued that the shallow-water definition, F_i, is the most deserving of the title. Given the analogy between the flows studied in this paper and shallow-water flow, we shall adopt the latter convention throughout.

The remainder of this paper is set out as follows. A brief description of the numerical model and the configuration of the simulations is presented in section 2. Examples of results from the simulations are presented in section 3 and flow-regime diagrams are constructed in section 4. A linear theory for flow in the presence of a sharp temperature inversion is derived in section 5 and the theory is used to help interpret the numerical results. Conclusions are drawn in section 6.

2. Configuration of the numerical simulations

Numerical simulations were conducted with the Met Office BLASIUS code (Wood and Mason 1993). This model has been used extensively for studies of boundary-layer flows over small or moderate sized hills (e.g. Wood 1995; Ross and Vosper 2003). The model solves the time-dependent Boussinesq or anelastic equations in a terrain-following coordinate system (Gal-Chen and Somerville 1975) whose levels follow the mountain shape close to the surface and become horizontal at the model upper boundary. The equations are discretized using finite differences; a second-order accurate scheme is used for advection of velocity (Piacsek and Williams 1970) and the Leonard *et al.* (1993) Ultimate-Quickest scheme is used for advection of potential temperature. The results presented here were obtained using the Boussinesq equations and a first-order Richardson number dependent mixing-length turbulence closure scheme. Some limited tests with a $1\frac{1}{2}$ order closure scheme involving a transport equation for the turbulent kinetic energy (Belcher and Wood 1996) revealed that the details of the closure scheme had little impact on the results.

At the lower boundary, either a no-slip condition was imposed (via a similarity condition for the surface stress) or, alternatively, the ground was assumed to be frictionless and a free-slip condition was applied (following Durran and Klemp 1983). Comparison of no-slip and free-slip simulations then allowed the impact of surface friction and the presence of a developed upstream boundary layer to be investigated. Note that the turbulence parametrization was retained in the free-slip simulations in order to represent mixing above the surface, due to wave breaking for example. A zero surface heat-flux condition was applied at the lower boundary in both the free-slip and no-slip cases. For the free-slip simulations the model domain consisted of 1024 grid points in the x (streamwise) direction, whereas 512 grid points were used in the no-slip simulations. In all cases the vertical grid was stretched, with fine resolution near the surface, and consisted of 150 levels. The lowest grid point above the ground was at 2 m. The vertical grid spacing increased smoothly with height from 4 m to 324 m adjacent to the upper boundary, which was placed at 20 km. The horizontal resolution in all simulations was 125 m. In the no-slip simulations, a constant roughness length of 0.05 m was assumed, and the Coriolis force was imposed with $f = 10^{-4}$ s^{-1}. The inclusion of Coriolis force resulted in turning of the boundary-layer wind profile which was absent in the free-slip simulations and, of course, the introduction of friction and rotation into the problem increases the number of controlling parameters. The sensitivity of the flow to surface roughness and Rossby number ($R_o = \overline{U}/fL$) or Burger number ($B = (NH/fL)^2$) is beyond the scope of this study but, since $R_o \gg 1$ for the cases considered here, it seems likely that rotation will have little impact on the dynamics of the flow. Note that the Coriolis parameter was, in fact, omitted in the free-slip simulations. However, as we would expect given the lack of frictional turning of the background wind in the free-slip case, tests in which f was included resulted in little change to the flow.

A rigid-lid upper-boundary condition was applied and a Rayleigh damping layer was placed above 15 km in order to minimize the reflection of upward propagating gravity waves. The damping was applied to the perturbation velocity and potential-temperature fields, and the damping coefficient increased smoothly from zero at the bottom of the layer to a maximum value at the upper boundary.

Periodic lateral boundary conditions were applied in all simulations. In order to avoid wrap-around effects, additional Rayleigh damping was applied in 8 km wide columns adjacent to the upwind and downwind boundaries. As for the upper layer, the damping coefficient in these columns increased smoothly towards the boundaries.

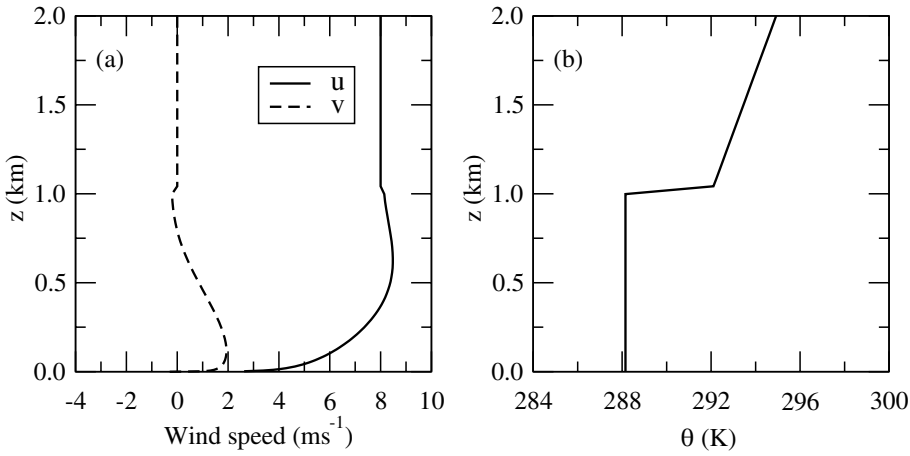

Figure 2. The profiles of (a) wind and (b) potential temperature used to initialize the 2-D no-slip simulations. For the case shown the geostrophic wind $(\overline{U}, \overline{V}) = (8, 0)$ m s^{-1}, the inversion height, z_i, is 1 km and $\Delta\overline{\theta} = 3.84$ K.

These damping columns proved to reduce wrap-around effects* effectively, although one side effect was the generation of grid-scale noise at their inner edges. It was found necessary to apply a small amount of fourth-order smoothing (Durran and Klemp 1983) to the perturbation velocity and potential-temperature fields to prevent the growth of such noise. This smoothing was applied along the model's terrain-following coordinate surfaces only; no smoothing was required in the vertical direction. Note that the choice of periodic boundary conditions combined with damping columns was preferred over the more natural choice of inflow–outflow conditions because tests with the latter suffered from the build-up of spurious noise near the boundaries.

The idealized ridge used in this study is of the form

$$h(x) = \begin{cases} H\{1 + \cos(Kx)\}/2 & \text{for } |x| \leqslant \pi/K \\ 0 & \text{for } |x| > \pi/K, \end{cases} \tag{3}$$

where $K = 2\pi/L$ and $x = 0$ is the centre of the model domain. The initial basic-state profiles of wind and potential temperature were as described in section 1. These consisted of a constant westerly geostrophic wind, $(\overline{U}, 0)$ and a two-layer Brunt–Väisälä frequency profile. In the lowest layer the stratification was neutral and the upper layer was stably stratified with a typical tropospheric value for the Brunt–Väisälä frequency ($N = 0.01$ s^{-1}). The discontinuity in potential temperature between the two layers was represented by imposing a jump, of size $\Delta\overline{\theta}$, across a single grid level. Depending on the height relative to the ground at which this was imposed, the grid spacing across the jump varied between about 20 m and 70 m for inversions located at 400 m and 1600 m, respectively. In cases where the no-slip lower-boundary condition was applied a one-dimensional (1-D) boundary-layer solution was first obtained using a 1-D version of the model which was run to a steady state. This resulted in a modification to the wind profile in the lower layer (i.e. beneath the inversion) but, because of the Richardson number dependency in the turbulence scheme, the potential-temperature structure was unaltered. Examples of these boundary-layer profiles are shown in Fig. 2.

* Comparisons of otherwise identical simulations with 512 and 1024 grid points in the horizontal showed that the flow near the mountain was insensitive to the position of the damping columns relative to the mountain.

Simulations were conducted for a range of inversion strengths ($\Delta\overline{\theta}$) and inversion heights (z_i), and in all but a few cases the values of $\overline{U}$, N and L were fixed at 8 m s^{-1}, 0.01 s^{-1} and 10 km, respectively, thus fixing the value of F_L at 0.08. Since $F_L \ll 1$, gravity-wave motion in the stable layer above the inversion will be hydrostatic to a good approximation. Note also that the chosen value L means that 80 grid points span the width of the mountain, and thus the flow in this region is very well resolved. In all but a few cases the hill height, H, was also fixed and, unless otherwise stated, it should be assumed that $H = 400$ m. The 2-D simulations were initialized with the 1-D profiles and the integration was generally for 30 000 s, by which time transient disturbances generated during the initial stages of the flow evolution had disappeared.

3. Model results

In this section we present results for a range of different inversion strengths, $\Delta\overline{\theta}$, and heights, z_i, whilst keeping the hill height and width and all other flow properties fixed. The values of $\overline{U}$, H, N and L chosen for these simulations are described in section 1. For these values, $F_L = 0.08$, $S = 0.04$ and $NH/\overline{U} = 0.5$. The specific results presented have been chosen in order to demonstrate the wide variety of flow types which can occur, and the sensitivity of the flow to the inversion height and strength. The results are presented in terms of the Froude number, F_i, and the ratio of mountain height to inversion height, H/z_i.

(*a*) *Vertically propagating mountain waves:* $F_i = \infty$

We begin by examining a case in which no inversion is present, i.e. $\Delta\overline{\theta} = 0$ K. Figure 3 shows the flow field in the free-slip case (i.e. no boundary layer is present) for which $z_i = 400$ m ($H/z_i = 1$) at a time $t = 24L/\overline{U}$ (30 000 s). Although there is no inversion, the parameter z_i is still of some importance since it is the depth of the neutral layer immediately above the ground. As we might expect, Fig. 3 reveals that, above the neutral layer, a vertically propagating wave is present over the mountain. Note that the amplitude of the wave is not sufficient for wave breaking to occur above the mountain and, although not shown here, results obtained with shallower neutral layers also show no sign of wave breaking. There is, however, a clear increase of wave amplitude as z_i decreases and the wave amplitude is greatest in the case where no neutral layer is present at all ($z_i = 0$). The absence of wave breaking is not surprising, since here the non-dimensional mountain height, $NH/\overline{U}$, is considerably less than unity. Identical simulations (not shown) conducted with the no-slip boundary condition also show no evidence for wave breaking and, in these cases, the wave amplitude is slightly reduced relative to the free-slip simulations. The absence of wave breaking is consistent with the results of Lin and Wang (1996), who found that wave breaking did not occur for $NH/\overline{U} \lesssim 0.89$ in flow with constant upstream N and $\overline{U}$ over a 2-D ridge.

(*b*) *Lee waves on the inversion:* $H/z_i = 0.25$, $F_i = 0.6$

Figure 4 shows the steady-state flow field (at $t = 24L/\overline{U}$) resulting from a simulation in which the no-slip boundary condition was applied. In this case the inversion strength and height were 3.26 K and 1600 m, respectively, and thus $H/z_i = 0.25$ and $F_i = 0.6$. A region of maximum wind speed, shifted slightly downstream of the mountain summit, is present above the mountain and this extends throughout the neutral layer up to the height of the inversion. As for the $F_i = \infty$ case, the flow above the inversion contains a vertically propagating wave which is located immediately above the

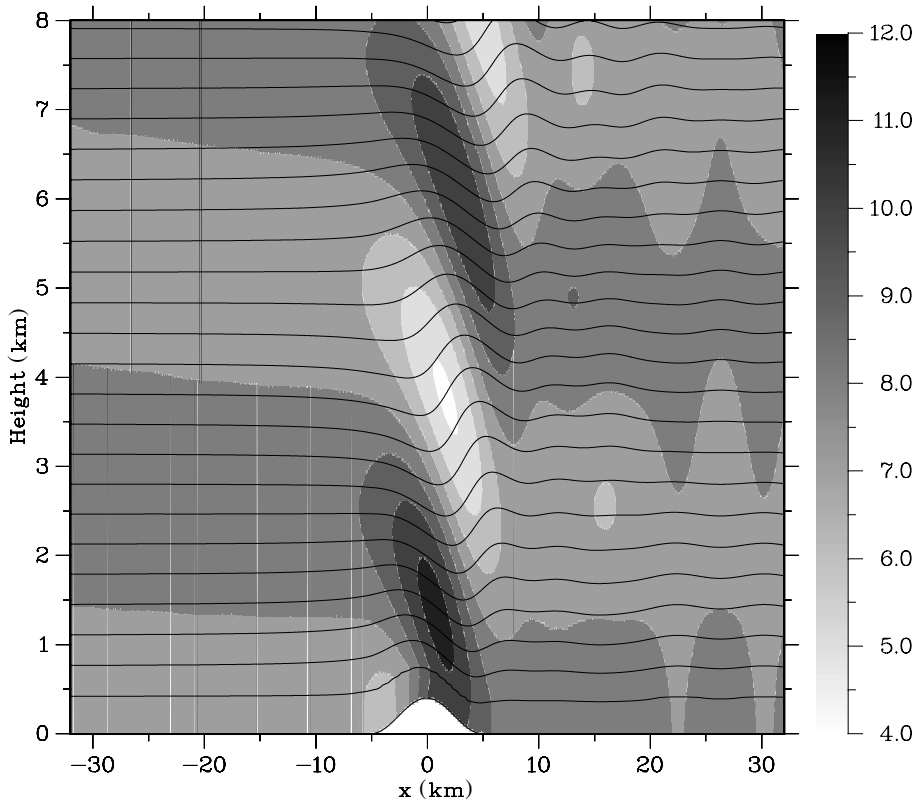

Figure 3. The flow field after an integration time of $24L/\overline{U}$ for a free-slip simulation in which no inversion is present ($F_i = \infty$). The height of the neutral layer, z_i, is 400 m. Quantities shown are the x velocity component (shaded contours, units m s^{-1}) and potential temperature (line contours, interval 1 K). See text for further details.

mountain. In this case, however, an additional stationary short-wavelength disturbance is present downwind of the mountain. This wave train resembles a trapped lee-wave disturbance of the kind normally associated with the presence of a wave guide due to vertical variations of wind speed and stability (e.g. Scorer 1949; Sawyer 1960). The lee-wave train has a maximum amplitude on the inversion and extends far downwind without any significant reduction in amplitude. The wavelength of the disturbance is around 4.8 km. Note that the introduction of the free-slip condition in place of the no-slip lower boundary condition has only a subtle impact on the flow shown in Fig. 4. The wavelength of the lee wave appears to be quite insensitive to the choice of boundary condition; the free-slip boundary condition causes a reduction in the wavelength of less than 2.5%. The wave amplitude is more sensitive however. The mean maximum value of the vertical velocity at the inversion height downwind of the mountain is increased by 28% when the no-slip condition is replaced by free-slip.

Although not shown here, results from a no-slip simulation with a slightly stronger inversion ($\Delta\overline{\theta} = 7.35$ K, $F_i = 0.4$), but for the same inversion height, reveal that a lee wave is again present on the inversion. In this case, however, the horizontal wavelength of the disturbance is somewhat shorter at around 3.2 km. Examination of results for a range of values of F_i, but fixed inversion height, reveal a general trend for the horizontal wavelength to decrease with decreasing F_i. This is discussed further in section 5.

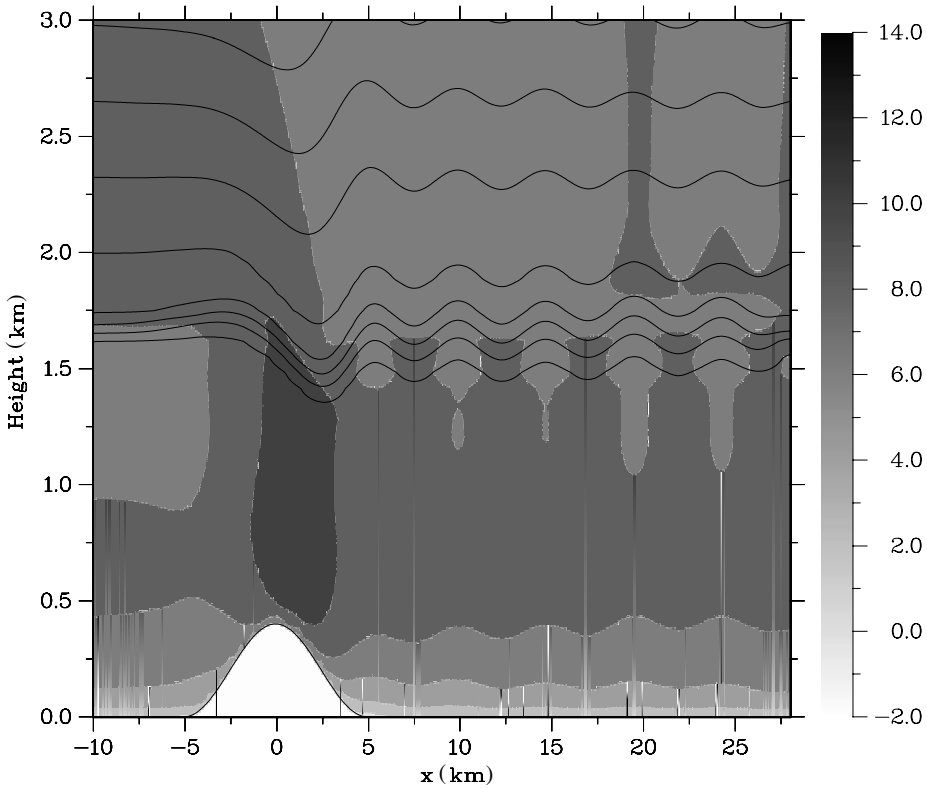

Figure 4. As Fig. 3, but for a no-slip simulation with $F_i = 0.6$ and $H/z_i = 0.25$. The dimensional parameters for this simulation are $\Delta\overline{\theta} = 3.26$ K, $z_i = 1600$ m, $\overline{U} = 8$ m s^{-1} and $H = 400$ m. Note that only a small part of the model domain is shown here.

(*c*) *Lee-wave rotors and wave breaking:* $H/z_i = 0.5$, $F_i = 0.6$

Figure 5 shows the flow fields for the no-slip simulation in which $\Delta\overline{\theta} = 6.53$ K ($F_i = 0.6$) and $z_i = 800$ m ($H/z_i = 0.5$) at $t = 24L/\overline{U}$. As in the $z_i = 1600$ m case at the same Froude number (Fig. 4) a short-wavelength disturbance occurs on the inversion downwind of the mountain. When $z_i = 800$ m, however, the amplitude of the wave field is sufficient to force large amplitude perturbations in the boundary layer beneath the inversion. Indeed, the flow can be seen to reverse underneath the wave crests, overturning occurs and regions of closed recirculation, or rotors, are present. Figure 6, which shows a close-up of the cross-stream (y) component of vorticity immediately downwind of the mountain, illustrates a similar phenomenon to that demonstrated by Doyle and Durran (2002). Namely a thin layer of high (positive) vorticity is present close to the lee slope of the mountain due to the friction at the ground. This vorticity appears to be swept up away from the surface and into the first rotor as the flow separates at the foot of the mountain underneath the first lee-wave crest. Further downwind ($x \sim 7$ km), underneath the first lee-wave trough, a new region of high positive vorticity is formed as the near-surface flow is accelerated. This vorticity is subsequently swept up into the interior of the flow as the flow separates upwind of the second rotor. This continues downstream under further lee-wave crests.

Also shown in Fig. 6 is the horizontal pressure gradient, $\partial p'/\partial x$, where p' is the perturbation (mountain induced) pressure. The location of flow separation at the

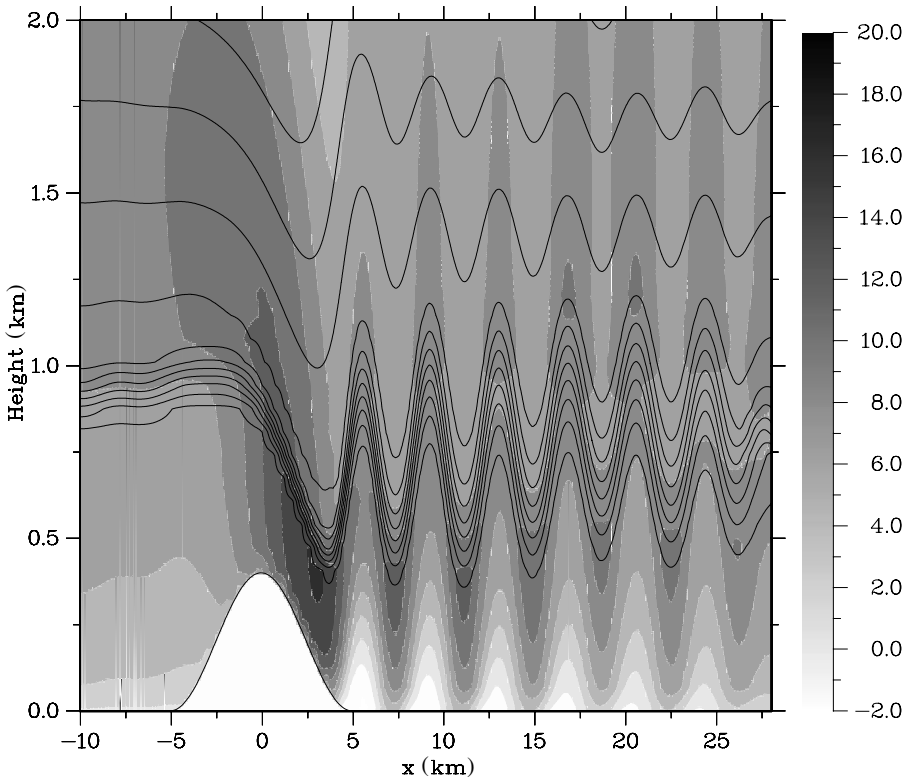

Figure 5. As Fig. 4, but for a no-slip simulation with $F_i = 0.6$ and $H/z_i = 0.5$ ($\Delta\overline{\theta} = 6.53$ K, $z_i = 800$ m).

upwind edge of the first rotor ($x \sim 4$ km) appears to coincide approximately with a local (positive) maximum in the horizontal pressure gradient. This is also true at the upwind edges of successive rotors downwind and the maxima in $\partial p'/\partial x$ are themselves associated with the lee-wave train. This is consistent with the findings of Doyle and Durran (2002) who showed that there was a strong correlation between lee-wave amplitude (and hence lee-wave induced pressure gradient) and the strength of reversed flow in the rotors. As discussed by Doyle and Durran (2002), it is well known that the boundary layer will separate from the lee-slope of an obstacle when a positive (adverse) pressure gradient exists that is sufficiently large to cause flow reversal near the surface. Wood (1995) has shown that this occurs in neutral flow over a hill when the slope and/or the surface roughness are sufficiently high. Figure 6 and Doyle and Durran's results, however, serve to illustrate that in stratified conditions flow separation can occur a considerable distance away from the hill itself, where the terrain is flat. In this case the pressure field forcing the separation is associated with the lee-wave field, and the occurrence of separation is not directly linked to the mountain slope.

Given the apparent importance of surface friction in this case, it is interesting to compare these results with the equivalent free-slip simulation. Unlike the previous lower H/z_i case (see section 3(b)), here we find that the change of boundary condition makes a significant difference. Firstly, no flow separation occurs underneath the lee-wave crests, and hence no closed rotor circulations form. Secondly, the lee-wave field itself is unsteady and propagates downwind away from the mountain. Figure 7 shows

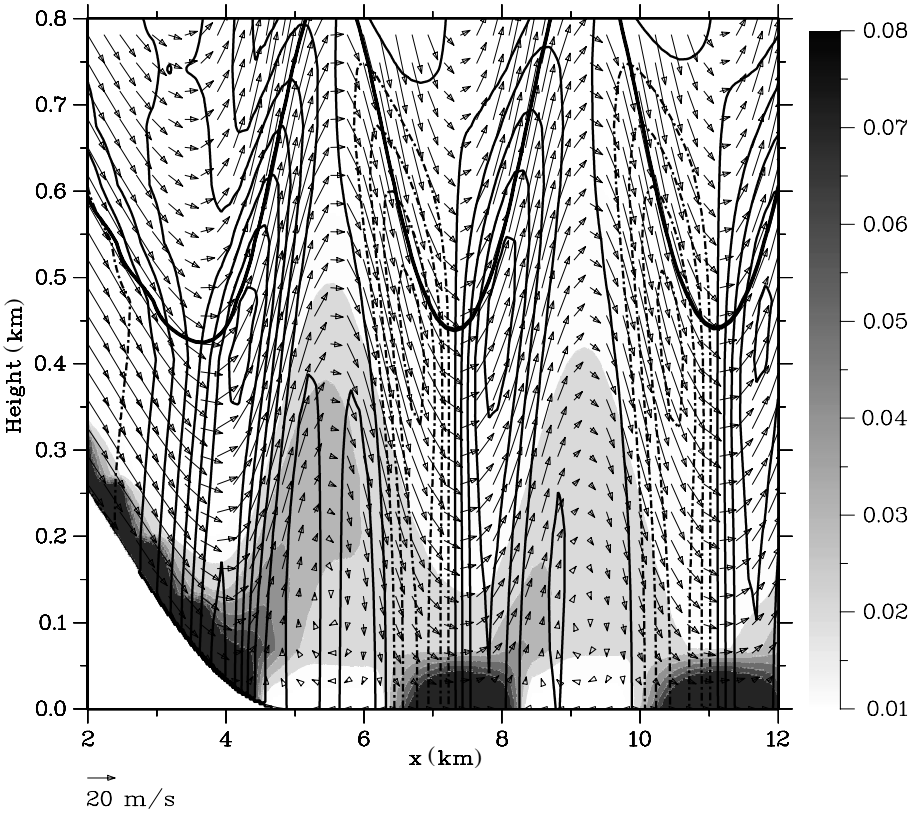

Figure 6. A close-up view of the near-surface flow shown in Fig. 5. Quantities shown are the cross-stream vorticity component (shaded contours s^{-1}), wind vectors and the horizontal pressure gradient, $\partial p'/\partial x$, (line contours with interval 0.01 Pa m^{-1}). Negative values of $\partial p'/\partial x$ are denoted by dashed contours and solid lines denote regions where $\partial p'/\partial x \geqslant 0$. Also shown is the 289 K potential-temperature contour (thick bold line), which marks the location of the inversion. Note only positive vorticity values are displayed to help illustrate the transfer of frictionally generated vorticity away from the surface where the flow separates.

the flow field at a time $t = 12L/\overline{U}$. As in the no-slip case, a lee-wave train is present at the inversion height. The horizontal wavelength of this wave train differs from that in the no-slip simulation by less than 3% although the amplitude (measured by the magnitude of the maximum vertical velocity at the inversion height) is almost 30% smaller. No separation occurs under the lee waves and therefore, as found by Doyle and Durran (2002), it would seem that friction plays a crucial role in the formation of lee-wave rotors. Note also that in Fig. 7 the first lee-wave crest is displaced a considerable distance downwind of the foot of the mountain. Animation of the flow after this time reveals that the whole wave train is in fact propagating slowly downstream and this coincides with the simultaneous growth of the vertically propagating wave immediately above the mountain. As shown by Fig. 7, by $t = 12L/\overline{U}$ this wave has grown large enough to force overturning at around 3 km and a region of stagnant flow is present over the mountain. As the flow continues to evolve the wave breaks down in this region and the lee-wave pattern continues to propagate downwind. No new lee waves are generated in the vicinity of the mountain. Note that, despite the apparent link in this particular case, wave breaking need not always be present in situations where lee waves

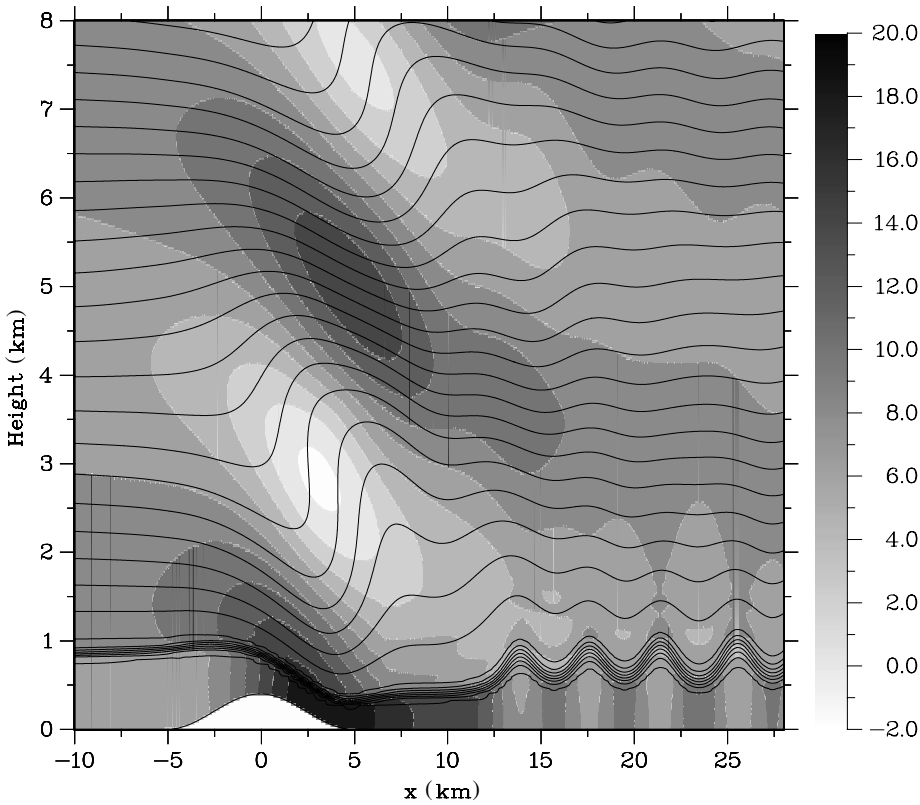

Figure 7. As Fig. 5, but for the free-slip simulation at $t = 12L/\overline{U}$ (15 000 s) of model integration time.

propagate downwind. Durran (1986), for example, has demonstrated that transient lee-wave development can occur in situations where only moderate-amplitude vertically propagating waves are present.

Although not shown here, the no-slip flow field equivalent to that of Fig. 5, but for a slightly stronger inversion with ($\Delta\overline{\theta} = 9.4$ K) and hence a reduced value of $F_\mathrm{i} = 0.5$, again exhibits a large-amplitude lee wave on the inversion which gives rise to rotors underneath the wave crests. Note, however, that the reduction in F_i leads to a steepening of the streamlines in the lee-wave field due to both an increase in the amplitude of vertical displacements and a shorter horizontal wavelength. As we see below, further decreases in Froude number will eventually lead to the wave field overturning downwind of the mountain.

(*d*) *Hydraulic jumps:* $H/z_\mathrm{i} = 0.5$, $F_\mathrm{i} = 0.4$

The flow field in a no-slip simulation at $t = 24L/\overline{U}$ for which $z_\mathrm{i} = 800$ m and $\Delta\overline{\theta} = 14.69$ K ($F_\mathrm{i} = 0.4$ and $H/z_\mathrm{i} = 0.5$) is shown in Fig. 8. The large-amplitude lee wave present at $F_\mathrm{i} = 0.6$ (see Fig. 5) has been replaced by a stationary hydraulic jump above the lee slope of the mountain. A region of overturning and stagnant flow can be seen immediately behind the jump which, beneath this the inversion layer itself, plunges down across the lee slope. A strong downslope wind is present below the inversion and at a height of 2 m above the ground the wind speed reaches 10.6 m s^{-1} half-way down the

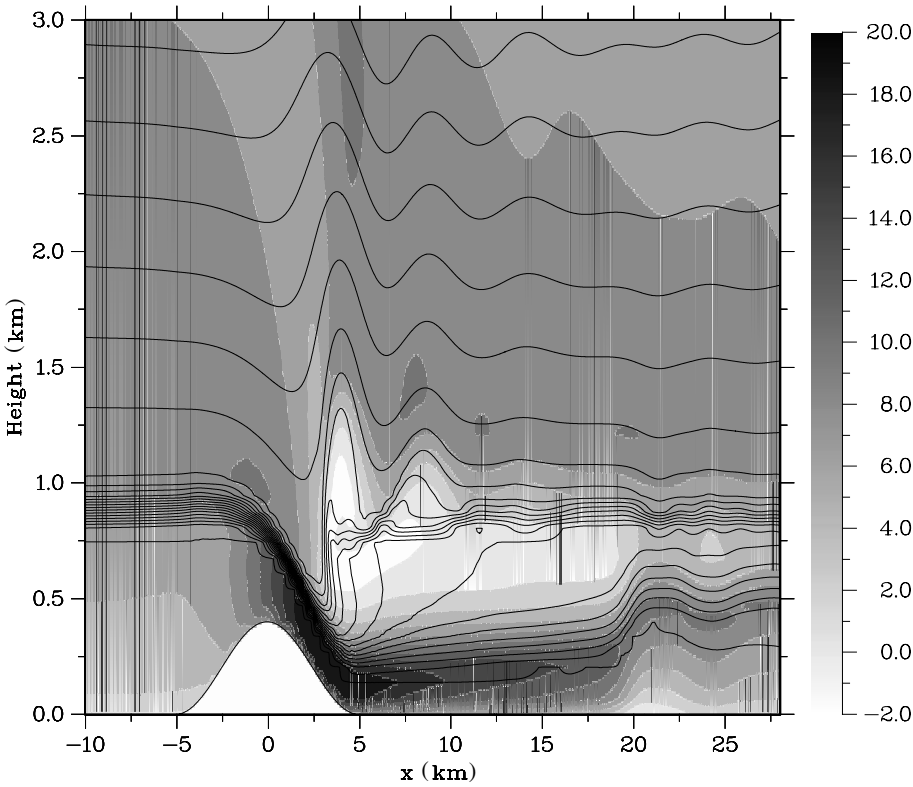

Figure 8. As Fig. 4, but for $F_i = 0.4$ and $H/z_i = 0.5$ ($\Delta\overline{\theta} = 14.69$ K and $z_i = 800$ m).

lee slope. This corresponds to an increase of about 370% relative to the upstream value at 2 m. It is interesting to note that, during the early stages of the evolution of this flow, a large-amplitude lee wave, similar to that seen at $F_i = 0.6$, starts to develop immediately downwind of the mountain. However, the amplitude of the wave is sufficiently large that overturning quickly occurs (by $t = 4L/\overline{U}$) and that, at this point, the lee-wave motion breaks down and is replaced by the hydraulic-jump feature.

Results obtained with the free-slip boundary condition in this case are qualitatively very similar to those obtained with the no-slip condition. A dramatic stationary hydraulic jump is again present over the lee slope of the mountain. The jump develops in the early stages of the flow evolution when a large-amplitude wave overturns immediately downwind of the mountain. The maximum in the 2 m wind over the lee slope again occurs approximately half-way down the lee slope.

4. THE FLOW REGIMES

A large number of simulations like those presented in section 3 have been used to generate regime diagrams for the flow types which occur with different inversion strengths and heights. Figure 9 shows the flow regime diagram for the no-slip simulations and the equivalent diagram for the free-slip case is shown in Fig. 10. Note that, as in section 3, variation in F_i and H/z_i is achieved by varying z_i and $\Delta\overline{\theta}$. The values of H, L, $\overline{U}$ and N, and hence F_L, $NH/\overline{U}$ and S, are again fixed and take the previously defined values.

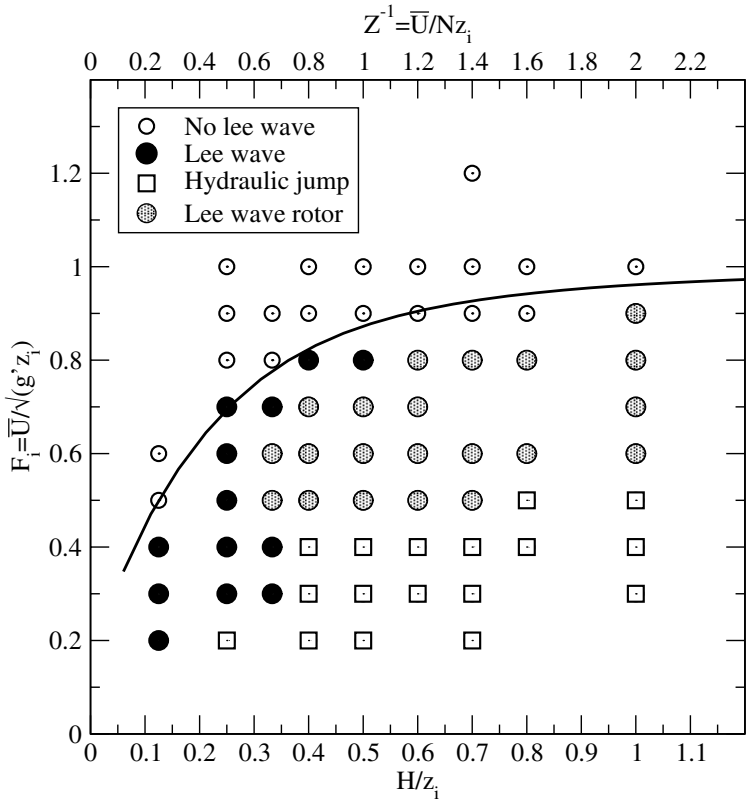

Figure 9. The regime diagram showing the $F_{\rm i}$ and $H/z_{\rm i}$ dependence of the flow when the no-slip lower boundary condition is applied. The non-dimensional parameters $F_L = \overline{U}/NL$, $NH/\overline{U}$ and $S = H/L$ are fixed at 0.08, 0.5 and 0.04, respectively. Also shown (solid curve) is the linear prediction of the maximum Froude number for which a steady trapped lee-wave field is present on the inversion (Eq. 17).

Three different flow regimes have been identified for the no-slip case. These are the lee-wave flows of the type shown in section 3(b), the hydraulic-jump flows (section 3(d)) and the regime in which only an upward propagating mountain wave is present above the mountain and no lee waves or hydraulic jumps occur (section 3(a)). As shown by Fig. 9, the latter regime occurs for sufficiently high values of $F_{\rm i}$. It appears that the critical value of $F_{\rm i}$ below which lee waves may occur falls with decreasing $H/z_{\rm i}$ (or alternatively increasing $Z = Nz_{\rm i}/\overline{U}$). This is discussed further in section 5 where linear theory is used to predict this critical Froude number. The lee-wave regime itself can be subdivided into two distinct regions: flows in which the wave amplitude is large enough so that rotors form beneath the wave crests, and flows in which the waves have too weak an amplitude for rotor formation. Figure 9 reveals that rotors will occur when $H/z_{\rm i} \gtrsim 0.3$ and when $F_{\rm i}$ is greater than about 0.5 but less than the critical value required for lee-wave formation. In general, for a sufficiently large fixed value of $H/z_{\rm i}$ ($\gtrsim$0.4), as the Froude number decreases the lee-wave field is eventually replaced by a stationary hydraulic jump. Figure 9 indicates that this occurs when $F_{\rm i}$ falls below about 0.4.

The regime diagram for the free-slip flows (see Fig. 10) is broadly similar to that in the no-slip case. Here, however, we can identify four distinct flow types. These are the three regimes that were identified in the no-slip case plus a wave-breaking regime in which the vertically propagating wave located above the mountain overturns. As seen

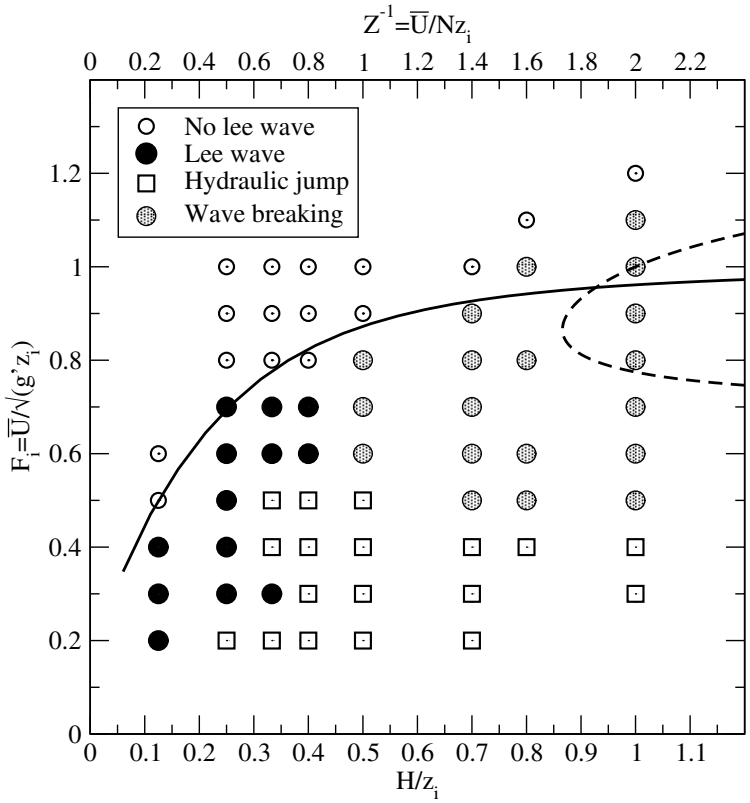

Figure 10. As Fig. 9, but for the free-slip simulations. Also marked (dashed curve) is edge of parameter space described by inequality (22), to the right of which linear theory predicts wave breaking above the inversion in the hydrostatic limit.

in the example of section 3(c) ($H/z_i = 0.5$, $F_i = 0.6$), the wave breaking has a major influence on the near-surface flow and tends to dominate over other features, such as the trapped lee wave or hydraulic jump. Indeed, the initial stages of all the wave-breaking simulations show the formation of either a transient lee wave or a hydraulic jump that is subsequently swept downstream as the mountain wave aloft grows in amplitude. Figure 10 reveals that the wave-breaking regime occurs for values of F_i greater than around 0.5 and for $H/z_i \gtrsim 0.5$. There also appears to be an upper limit to the Froude number for which wave breaking can occur, and this increases with increasing H/z_i; wave breaking is present for values of F_i up to 0.8 when $H/z_i = 0.5$, and for F_i as high as 1.1 when $H/z_i = 1$. Note that, for the region of parameter space examined here, wave breaking is entirely absent in the no-slip simulations. Although this has not been investigated further, it seems likely that this is due to a reduction in amplitude of the vertically propagating wave caused by the presence of the boundary layer.

Figure 10 indicates that, as for the no-slip flows, there is a critical Froude number above which lee waves cannot form on the inversion. Note, however, that, unlike the no-slip case, no flow separation occurs under the wave crests and consequently no rotors form. For sufficiently small F_i the lee wave is again replaced by a stationary hydraulic jump above the lee slope. Comparison of Fig. 10 with Fig. 9 suggests, however, that hydraulic jumps occur for smaller values of H/z_i and higher F_i in the absence of surface friction. This is presumably because the lee-wave amplitude is generally smaller when

the boundary layer is present (see section 3(b)) and thus, relative to the free-slip case, overturning will be delayed as F_i is reduced or H/z_i is increased.

5. Linear theory

We now turn our attention to obtaining solutions to the linearized equations of motion in an attempt to explain some of the features observed in the simulations. Clearly the quantitative predictions made by linear theory may be of limited use since the dynamics of phenomena, such as wave breaking, lee-wave rotors and hydraulic jumps, are highly nonlinear. We might hope, however, that linear theory will help to elucidate the important physical processes which may eventually lead to such phenomena.

We restrict attention to Boussinesq flow over 2-D ridges normal to the flow and assume solutions take the form

$$\phi'(x, z) = \frac{1}{2\pi} \int_{-\infty}^{+\infty} \widehat{\phi}(k, z)\, \mathrm{e}^{\mathrm{i}kx}\, \mathrm{d}k, \tag{4}$$

where $\phi' = (u', w', p', \theta')$ and u', w', p' and θ' are the perturbations to the horizontal velocity, vertical velocity, pressure and potential temperature, respectively. The function $\widehat{\phi} = (\widehat{u}, \widehat{w}, \widehat{p}, \widehat{\theta})$ gives the complex Fourier components of the wave field and k is the horizontal wave number. For simplicity we ignore boundary-layer effects here and restrict attention to free-slip flows in which, due to the absence of friction, the upwind velocity is independent of height. The vertical structure equation for each Fourier component of the vertical velocity in either layer is

$$\frac{\mathrm{d}^2 \widehat{w}_j}{\mathrm{d}z^2} + \left(\frac{N_j^2}{\overline{U}^2} - k^2 \right) \widehat{w}_j = 0, \tag{5}$$

where the subscript $j = 1$ or 2, and denotes either layer 1, the layer below the inversion, or layer 2, the upper layer. Note that, unlike in Klemp and Lilly's (1975) study, the form of Eq. (5) adopted here is valid for non-hydrostatic gravity waves and the hydrostatic approximation has not been made. As shown below, allowing for non-hydrostatic modes is an important aspect of this work, since it allows the existence of resonant lee-wave modes such as those seen in section 3. For mathematical convenience we define a new height coordinate, $z' = z - z_i$, such that the inversion occurs at $z' = 0$ and the ground is at $z' = -z_i$. Solutions to Eq. (5) take the form

$$\widehat{w}_1 = A_1\, \mathrm{e}^{\mathrm{i}m_1 z'} + B_1\, \mathrm{e}^{-\mathrm{i}m_1 z'} \tag{6}$$

and

$$\widehat{w}_2 = A_2\, \mathrm{e}^{\mathrm{i}m_2 z'}, \tag{7}$$

where A_1, B_1 and A_2 are complex constants to be determined via boundary conditions and matching conditions at the inversion. Equation (6) expresses the fact that, due to reflection at the inversion, solutions in the lower layer contain contributions from both upward and downward propagating waves, whereas the absence of shear or variation in N in the upper layer means that Eq. (7) contains only an upward propagating contribution. The quantities m_j are vertical wave numbers and are given by

$$m_j^2 = \frac{N_j^2}{\overline{U}^2} - k^2, \tag{8}$$

and, for any given wave number k, the choice of sign of m_2 and m_1 are governed by either upward group-velocity arguments or the choice of exponential decay of the upward propagating solution.

The appropriate matching conditions at $z' = 0$ are obtained by requiring that the vertical velocity and pressure are continuous across the inversion. Following Klemp and Lilly (1975) these conditions can be written as

$$\left.\begin{aligned} \widehat{w}_1 &= \widehat{w}_2 \\ \frac{\mathrm{d}\widehat{w}_1}{\mathrm{d}z'} - \widehat{w}_1\frac{g'}{\overline{U}^2} &= \frac{\mathrm{d}\widehat{w}_2}{\mathrm{d}z'} \end{aligned}\right\} \quad \text{at} \quad z' = 0, \tag{9}$$

and the details of the derivation of the second matching condition are given in the appendix. The linearized lower boundary condition for the vertical velocity is $w' = \overline{U}\,\mathrm{d}h/\mathrm{d}x$. When Fourier transformed this becomes, for each mode,

$$\widehat{w}(z' = -z_\mathrm{i}) = \overline{U}\mathrm{i}\widehat{h}k, \tag{10}$$

where $\widehat{h}(k)$ is the Fourier transformed terrain function.

We now restrict attention to the case where the lowest layer is neutrally stratified (i.e. $N_1 = 0$) and, for consistency with previous notation, we henceforth refer to the stability in the upper layer simply as N, rather than N_2. From Eq. (8) we have $m_1^2 = -k^2$ and, to ensure exponential decay with height of the upward propagating contribution in the lower layer, we choose $m_1 = \mathrm{i}|k|$. Substitution of (6) and (7) into (9) and (10) then gives, after some algebraic manipulation,

$$\widehat{w}_1 = \overline{U}\mathrm{i}k\widehat{h}\,\frac{\widehat{f}(k, z')}{\widehat{f}(k, -z_\mathrm{i})} \tag{11}$$

and

$$\widehat{w}_2 = -2\overline{U}\mathrm{i}k\widehat{h}\,\mathrm{e}^{\mathrm{i}m_2 z'}\{\widehat{f}(k, -z_\mathrm{i})\}^{-1}, \tag{12}$$

where

$$\widehat{f}(k, z') = -2\left\{\cosh(|k|z') + \left(\frac{1}{F_\mathrm{i}^2|k|z_\mathrm{i}} + \frac{\mathrm{i}m_2}{|k|}\right)\sinh(|k|z')\right\}. \tag{13}$$

(*a*) *Resonant lee waves*

It is clear from Eq. (11) that a singularity occurs when $\widehat{f}(k, -z_\mathrm{i}) = 0$. Manipulation of Eq. (13) reveals that this occurs when

$$\left(\frac{1}{F_\mathrm{i}^2|k|z_\mathrm{i}} + \frac{\mathrm{i}m_2}{|k|}\right)\tanh(|k|z_\mathrm{i}) = 1. \tag{14}$$

These singularities correspond to the presence of stationary resonant wave modes (Sawyer 1960) whose amplitude is a maximum at $z = z_\mathrm{i}$ (i.e. on the inversion). Note that similar resonant modes occur when non-hydrostatic effects are accounted for in the flow of a single layer of fluid (bounded by a free surface) over an obstacle (Baines 1995). The dispersion relation for these interfacial waves is different, however, due to the lack of stable stratification in a fluid layer above the free surface.

Equating real and imaginary parts of Eq. (14) we can see that the upper-layer vertical wave number, m_2, for these resonant modes must be imaginary. For exponential decay above the inversion we then have $m_2 = \mathrm{i}(k^2 - N^2/\overline{U}^2)^{1/2}$ from Eq. (8) and

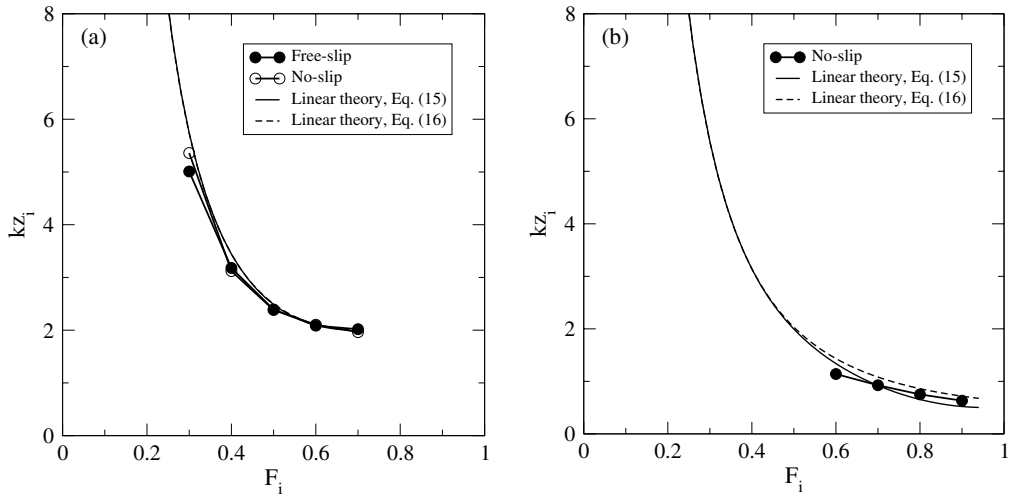

Figure 11. The variation of the lee-wave horizontal wave number with F_i in the free-slip and no-slip numerical simulations and the wave number predicted by linear theory when (a) $Z = 2$ and (b) $Z = 0.5$. Both the exact linear solution for the wave number (Eq. 15) and the approximate expression (Eq. 16) valid for $|k|z_\mathrm{i} \gg 1$ are shown. Note that the latter curve is obscured in (a) due to the close agreement with Eq. (15). Note also that only the no-slip numerical results are shown in (b) since no lee waves occurred in the free-slip simulations.

substitution into (14) then gives

$$F_\mathrm{i}^2 = \left[z_\mathrm{i} \left\{ \frac{|k|}{\tanh(|k|z_\mathrm{i})} + \left(k^2 - \frac{N^2}{\overline{U}^2} \right)^{1/2} \right\} \right]^{-1} . \tag{15}$$

Equation (15) provides an implicit formula for the resonant wave number, k. Note, however, that for $|k|z_\mathrm{i} \gg 1$, Eq. (15) can be rearranged to give the following explicit approximate expression for k:

$$|k|z_\mathrm{i} \approx \frac{1}{2} \left(\frac{1}{F_\mathrm{i}^2} + Z^2 F_\mathrm{i}^2 \right) , \tag{16}$$

where the non-dimensional inversion height, Z, is defined by Eq. (1).

Figure 11 shows the variation of kz_i with F_i for values of $Z = 2$ and 0.5, obtained both from iterative solutions to Eq. (15) and from the approximate expression, Eq. (16). It is clear that the approximation, valid for large $|k|z_\mathrm{i}$, is a good one for all values of F_i when $Z = 2$ and also for $Z = 0.5$ when F_i is sufficiently small; noticeable differences between the two curves are only apparent in Fig. 11(b) when $F_\mathrm{i} \gtrsim 0.6$. The $1/F_\mathrm{i}^2$ dependency in Eq. (16) implies a rapid increase of k as F_i falls towards zero. For larger values of F_i, $|k|z_\mathrm{i} \to Z$ as F_i increases, because the wave number cannot fall below $N/\overline{U}$. The consequence of this lower bound on k is discussed further below. Also shown in Fig. 11 are the values of kz_i diagnosed from all the no-slip and free-slip numerical simulations in Figs. 9 and 10 at $Z = 2$ ($H/z_\mathrm{i} = 0.25$) and $Z = 0.5$ ($H/z_\mathrm{i} = 1$) for which lee waves were present. For each simulation the wave numbers were determined from the mean wavelengths of disturbances in the velocity fields downwind of the mountain close to $z = z_\mathrm{i}$. It appears that linear theory provides an accurate prediction for the wavelength of the lee waves. This is true even for the no-slip $H/z_\mathrm{i} = 1$ flows, where rotors occur below the wave crests.

Note that, since F_i must be a real number, Eq. (15) provides an upper limit on F_i^2, above which resonance cannot occur. The physical reason for this is simply that, for horizontal wave numbers smaller than $N/\overline{U}$, the waves are able to propagate freely in the vertical above the inversion and thus no trapping mechanism exists. Substituting $k = N/\overline{U}$ into Eq. (15) we find that we require

$$F_i^2 \leqslant \tanh(Z)/Z \tag{17}$$

for resonant waves to exist on the inversion. The critical value of F_i implied by this inequality is plotted on both regime diagrams in Figs. 9 and 10. No lee waves appear to occur when F_i is greater than this critical value. This is true in both the free-slip and no-slip flows and it appears that linear theory provides a useful prediction of when we can expect resonant lee waves, and possibly rotors, to occur.

The solution for the vertical-velocity field is obtained by substitution of (6) and (7) into the integral (4). The resonant-mode contributions then give rise to simple poles which lie on the real k-axis. Following Sawyer (1960), we take the contour of integration around the poles below the real axis to obtain a solution valid far downstream of the mountain. The resonant downstream contribution to the wave field is given by

$$w'(x, z') = -\overline{U} \left\{ \frac{\widehat{f}(k_r, z')}{\widehat{f}'(k_r, -z_i)} k_r \widehat{h}(k_r)\, e^{ik_r x} + \text{complex conjugate} \right\}, \tag{18}$$

where $\widehat{f}' = \partial \widehat{f}/\partial k$ and k_r is the positive resonant wave number (i.e. the positive solution to Eq. (15)) and the contribution from the complex conjugate comes from the negative wave number contribution.

The linear prediction of the lee-wave amplitude has been computed from Eq. (18) and compared with the numerical results. The Froude number dependence of the maximum vertical velocity given by Eq. (18) at $z = z_i$ is shown in Fig. 12 for an inversion height of 1600 m. The vertical velocity shown has been normalized by the factor $\overline{U}H/L$. Also shown are the maximum vertical velocities downwind of the mountain on the inversion from the relevant no-slip and free-slip simulations discussed in section 3(*b*). Although both numerical results and linear theory predict a maximum in the normalized vertical velocity at a Froude number of around 0.5, the linear theory clearly significantly underestimates the wave amplitude at all Froude numbers. Also shown in Fig. 12 are the results from an additional series of free-slip simulations in which the hill height was reduced from 400 m to 20 m ($H/z_i = 0.0125$). It appears that, in this case, the agreement with the linear theory is more reasonable.

The discrepancy between the linear-theory wave amplitude and that observed in the numerical simulations has been investigated further by conducting a series of free-slip simulations with different mountain heights. Figure 13 shows the ratio of maximum lee-wave vertical velocity on the inversion in the simulations to that predicted by linear theory. Results are presented for two different sets of simulations, with inversion heights of 1600 m and 3200 m. The Froude number is fixed at 0.6 for all simulations and by choosing different values of $\overline{U}$, namely 8 and 16 m s^{-1} for the $z_i = 1600$ m and 3200 m simulations, respectively, the non-dimensional inversion height is also fixed at $Z = 2$. Figure 13 shows that, for sufficiently small hill heights, there is close agreement between the numerical results and linear theory for both values of z_i. This is true for mountains at least as high as 400 m when the inversion height is 3200 m. When z_i is reduced to 1600 m, however, the results diverge rapidly for hill heights greater than only about 50 m and it would seem that the lee-wave amplitude is controlled by nonlinear

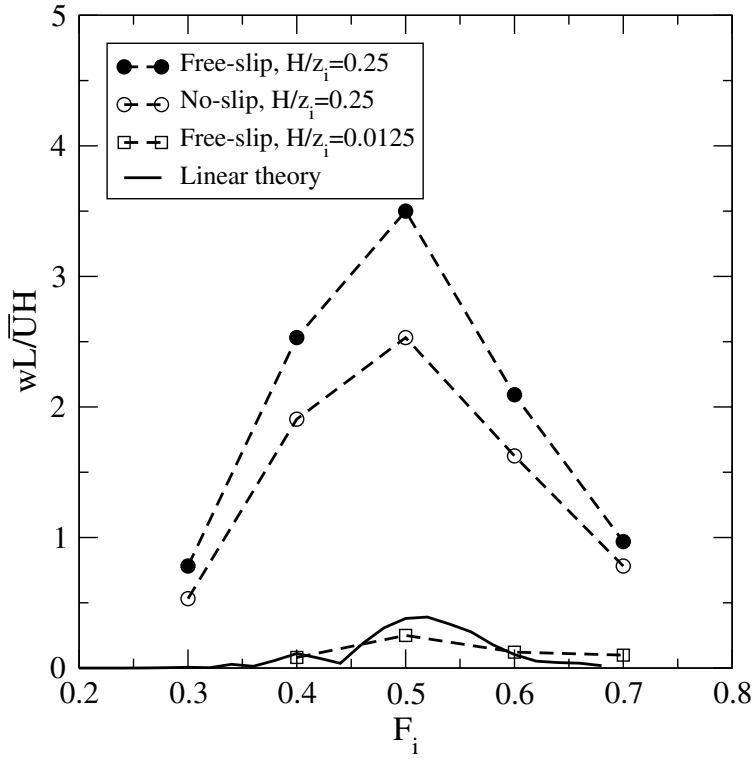

Figure 12. The variation of the lee-wave maximum normalized vertical velocity at the inversion height with F_i. Results shown are for a fixed inversion height ($z_i = 1600$ m) and mountain heights of 400 m and 20 m. Both free-slip and no-slip results are shown, as well as the linear theory prediction, Eq. (18).

processes for only moderate size hills. Note that this effect has also been demonstrated for situations where no inversion is present. The work of Smith (1976) and Durran and Klemp (1982), for example, clearly shows that, in some situations, linear theory seriously underestimates the amplitude of trapped lee waves.

One effect of reducing the inversion height whilst keeping F_i and Z fixed is to reduce the horizontal wavelength of the lee waves on the inversion; solutions to Eq. (15) for $z_i = 3200$ m and 1600 m are $k = 0.654$ km^{-1} and 1.309 km^{-1}, respectively. Since, according to linear theory, the wave forcing is directly proportional to the hill Fourier transform at the resonant wave number (see Eq. 18), this change in wave number may have a significant impact on the linear wave amplitude. This is confirmed by examination of $\widehat{h}(k)$ for the cosine hill used in this study. A complicated analytic expression (not shown) for $\widehat{h}$ can easily be derived for this particular hill and, as shown by Fig. 14, as the wave number approaches 1.257 km^{-1} (which corresponds to a wavelength of $L/2$) the Fourier transform decreases rapidly with increasing k. The linear-wave amplitude is, therefore, very small for such wave numbers* and hence small in the $z_i = 1600$ m case. The fact that this is not the case in the simulations (and hence the ratio of nonlinear to linear wave amplitude is large for all but very low hills) is presumably because, in the absence of any direct forcing by the topography at the resonant wave number,

* The Fourier transform of the isolated cosine hill does, in fact, contain multiple zeros at $k = 2K$, $3K$, etc. These wave numbers correspond to wavelengths of $L/2$, $L/3$ etc.

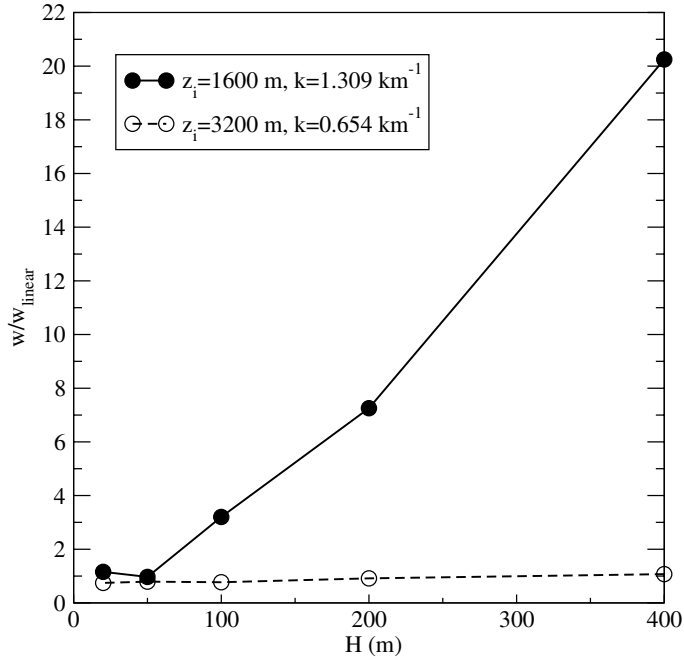

Figure 13. The variation with mountain height, H, of the ratio of lee-wave maximum vertical velocity at the inversion height in the free-slip simulations to that predicted by linear theory. Results shown are for a fixed Froude number, $F_{\mathrm{i}} = 0.6$, and for inversion heights of 1600 m and 3200 m. For all simulations $Z = 2$.

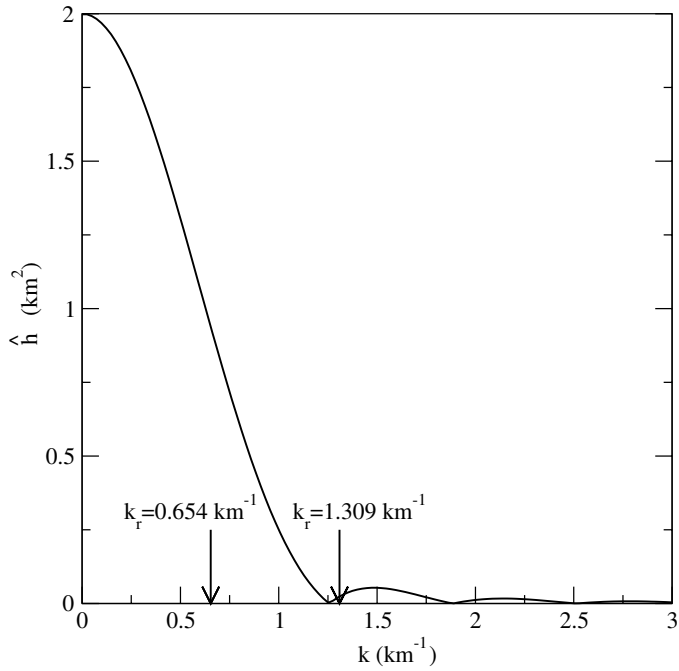

Figure 14. The Fourier transform, $\widehat{h}$, of the isolated cosine hill defined by Eq. (3) with $H = 400$ m and $L = 2\pi/K = 10$ km. Also marked are the resonant wave numbers, $k_{\mathrm{r}} = 1.309$ and $0.654\ \mathrm{km}^{-1}$ obtained from Eq. (15) when $F_{\mathrm{i}} = 0.6$, $Z = 2$ and $z_{\mathrm{i}} = 1600$ and 3200 m, respectively. Note $\widehat{h}$ is shown for positive k only.

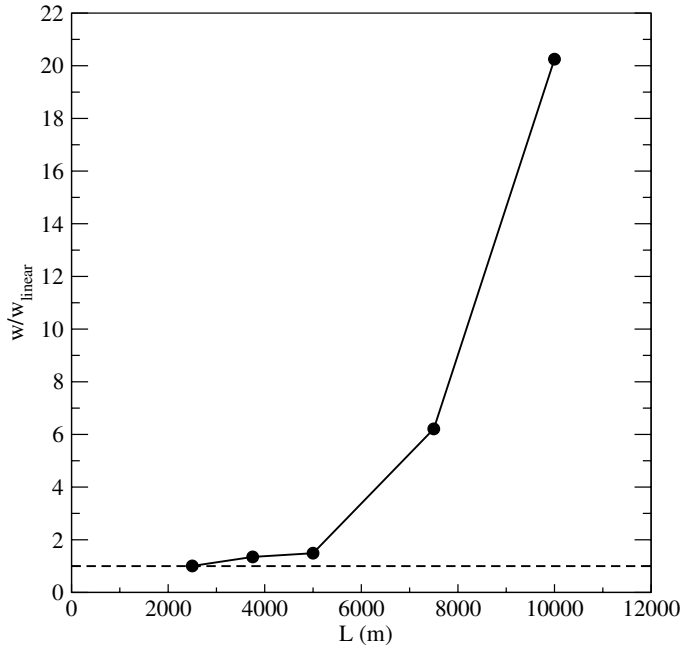

Figure 15. The variation with mountain width, L, of the ratio of lee-wave maximum vertical velocity at the inversion height in the free-slip simulations to that predicted by linear theory. For all simulations the values of z_i, F_i and Z are 1600 m, 0.6 and 2, respectively.

the wave amplitude is instead determined by nonlinear processes. This effect was also discussed by Durran (1992) who noted that linear theory can significantly underestimate the amplitude of trapped waves generated by wide mountains.

The above idea has been tested further by repeating the $z_i = 1600$ m free-slip simulations for a range of different mountain widths, L. In all cases H was fixed at 400 m. Figure 15 shows the variation of the ratio of nonlinear to linear lee-wave amplitude with L. As seen previously, for the higher values of L the nonlinear wave amplitude far exceeds the linear prediction. As L decreases, however, linear theory becomes increasingly accurate. For $L \lesssim 4.8$ km, for example, which corresponds to the resonant wavelength, the ratio of nonlinear to linear amplitude is less than 1.5. For $L = 2.5$ km the ratio is close to unity. It would seem, therefore, that linear theory does provide a useful prediction of wave amplitude provided the ratio of hill width to lee wavelength is less than about 1. Note that Yang and Akylas (1996) obtained a similar result for lee waves generated in the flow of a continuously stratified fluid (with constant N and $\overline{U}$) in a channel of finite depth. Yang and Akylas found that finite-amplitude effects dominate when ϵ/μ^p is of order unity, where ϵ is the ratio of hill height to channel depth, μ is the ratio of channel depth to hill width and p is a positive number dependent on the hill shape. For mountains that are wide compared with the channel depth ($\mu \ll 1$), the lee wavelength is comparable to the channel depth and, thus, their result implies that nonlinear effects become increasingly important as the ratio of wavelength to hill width decreases.

(*b*) *Upper-level gravity-wave breaking*

In the interests of understanding the wave breaking that occurs above the inversion in the free-slip simulations we now consider the vertically propagating wave solutions in the upper layer. For simplicity we restrict attention to the hydrostatic limit in which the vertical wave number $m_2 \sim N/\overline{U}$. For the flows considered in section 3 this approximation is valid since $F_L \ll 1$. For small k, Eq. (12) can be approximated by

$$\widehat{w}_2 = -\left(\frac{1}{F_i^2} + iZ - 1\right)^{-1} \overline{U} i\widehat{h}k \, e^{i(Nz'/\overline{U})}. \tag{19}$$

Equation (19) reveals that the amplitude of vertically propagating waves above the inversion will increase as the non-dimensional inversion height, Z, is reduced. We might, therefore, expect the waves to overturn for sufficiently small z_i. By application of the continuity equation an expression for $\widehat{u}_2(k, z)$, the Fourier transformed horizontal-velocity perturbation (u_2') in the upper layer, can be obtained:

$$\widehat{u}_2 = \frac{i\widehat{h}NF_i^2 \, e^{i(Nz'/\overline{U})}}{F_i^2(iNz'/\overline{U} - 1) + 1}. \tag{20}$$

The maximum value of u_2' in the upper layer can then be computed for any given mountain shape by substituting (20) into Eq. (4). This maximum value occurs at heights where $\tan(Nz'/\overline{U}) = ZF_i^2(1 - F_i^2)^{-1}$ directly above the mountain summit and be written as

$$|u_2'/\overline{U}| = \frac{NH}{\overline{U}} \left\{(1 - F_i^2)^2 + Z^2 F_i^4\right\}^{-1/2}. \tag{21}$$

The onset of wave breaking in the upper layer corresponds to the maximum value of $|u_2'/\overline{U}|$ being greater than unity. By manipulation of Eq. (21) it can be shown that linear theory predicts that wave breaking will occur whenever

$$\frac{H}{z_i} \geqslant \frac{NH}{\overline{U}} F_i^2 \left\{\left(\frac{NH}{\overline{U}}\right)^2 - (1 - F_i^2)^2\right\}^{-1/2}. \tag{22}$$

Note also that the square root on the right-hand side of (22) implies that we further require $|1 - F_i^2| < NH/\overline{U} = ZH/z_i$. The critical values of H/z_i and F_i implied by these inequalities are shown in the free-slip regime (Fig. 10). According to linear theory, wave breaking will occur to the right of the dashed curve. It is clear that, while linear theory might provide a qualitative description of the wave breaking, in reality overturning will occur for considerably lower values of H/z_i and F_i than predicted by the above inequalities. The lowest value of H/z_i for which overturning occurs in linear theory is around 0.867, whereas it is present in the free-slip simulations for H/z_i as small as 0.5. This discrepancy is by no means surprising since nonlinear effects will become important well before the actual onset of overturning.

6. Conclusions

This study has highlighted how the presence of a sharp temperature inversion upwind can have a significant impact on flow over mountains and illustrates how phenomena such as lee-wave rotors, hydraulic jumps and wave breaking can occur. For the idealized cases considered here, the flow behaviour is sensitive to the Froude number

and the height of the inversion. The formation of rotors is related to the presence of a resonant lee wave on the inversion downwind of the mountain. The wavelength and conditions under which this wave forms are well predicted by linear theory. This is true for both free-slip flows in which surface friction is neglected and for flows in which a boundary layer is present. The wave amplitude, however, is seriously underestimated by linear theory if the horizontal wavelength is significantly less than the hill length scale.

For fixed a Froude number, smaller than the critical value for the existence of lee waves on the inversion, results show that the lee-wave amplitude increases as the ratio of hill height to inversion height (H/z_i) increases. When boundary-layer friction is represented in the simulations, the amplitude can be large enough to cause flow separation. Closed rotor circulations then form underneath the wave crests. These rotors do not form when a free-slip boundary condition is applied however. In both the no-slip and free-slip simulations, as the Froude number is reduced the lee wave is eventually replaced by a stationary hydraulic jump above the lee-slope of the mountain. The results presented here indicate that hydraulic jumps will occur provided $H/z_i \gtrsim 0.25$. Note, however, that hydraulic jumps might also be present for smaller H/z_i, provided the Froude number is smaller than 0.2. No simulations have been designed to test this however.

One effect of neglecting surface friction in the numerical simulations is an increase in the amplitude of vertically propagating waves above the inversion, compared with those when a boundary layer exists. When the ratio of mountain to inversion height is greater than about 0.5 and the Froude number lies between around 0.5 and some upper limit (which increases with H/z_i) the wave amplitude is large enough to cause overturning above the mountain. Wave breaking then dominates the flow at low levels and lee waves, if they occurred in the early stages of flow development, are swept away downstream. Given that real atmospheric flows contain a boundary layer, it is tempting to infer that these free-slip simulations are unrealistic. One should bear in mind, however, that for mountains higher than those studied here the wave field may be of sufficient amplitude to break, regardless of whether a boundary layer is present or not. In such cases, the wave-breaking regime is likely to dominate the near-surface flow.

It is perhaps worth pointing out that in the context of atmospheric flow over mountains, the values of F_i, Z^{-1} and H/z_i in Fig. 9 for which rotors and hydraulic jumps occur, do not require extreme values of wind speed, mountain height and temperature change across the inversion. Consequently, such values will occur frequently in real situations. Routine radiosonde ascents from the Falkland Islands, for example, often contain sharp inversions starting at around 500 m with $\Delta\overline{\theta} \sim 10$ K or greater. Mountain heights on East Falkland are also typically 500 m and, assuming an upstream wind speed of 10 m s^{-1} and $N \sim 0.01$ s^{-1}, this then implies $F_i \sim 0.7$, $H/z_i \sim 1$ and $Z^{-1} \sim 2$. According to Fig. 9 we would expect lee-wave rotors to be present under these conditions. Recent near-surface wind measurements made on East Falkland (S. D. Mobbs, personal communication) reveal that episodes of dramatic downslope winds and flow reversal can occur for conditions such as these, which may indicate effects such as rotors or hydraulic jumps aloft. Clearly there is a need to properly relate field observations to the numerical results, but it seems likely that regime diagrams such as Fig. 9 could prove useful for forecasting damaging winds in mountainous terrain.

The results presented here have shown how flow over mountains is sensitive to the presence of a sharp temperature inversion. We should note, however, that the study has been restricted to the case of a discontinuity (or rather its finite difference representation) in potential temperature, whereas in reality inversions may occur over a depth of several hundred metres. Although a thorough investigation of the flow dependence on the

inversion depth is beyond the scope of this paper, some preliminary simulations, not presented here, have shown that the lee-wave wavelength has a tendency to increase with increasing inversion depth. Further, Klemp and Lilly's (1975) linear hydrostatic study demonstrated that the amplitude of the vertically propagating mountain wave increases as the inversion depth decreases. It seems possible, therefore, that in certain situations the whole character of the flow may change altogether when a sharp inversion is replaced by a much deeper one. This effect undoubtedly warrants further investigation. Perhaps more important, however, is the question of how the flow changes when the topography is three dimensional (3-D). It is well known that phenomena such as flow splitting and lee-vortex formation (e.g. Smolarkiewicz and Rotunno 1989; Schär and Durran 1997) occur in both shallow-water flows and flows with uniform N and $\overline{U}$ past axisymmetric 3-D mountains. Recent investigation of constant N and $\overline{U}$ flows past long 3-D ridges by Epifanio and Durran (2001) also reveals that the flow can be significantly different to that over 2-D ridges; the character of wave breaking and upstream flow blocking, for example, is sensitive to the length of the ridge. It seems likely that similar effects will be important when the work presented here is extended to 3-D flow.

Acknowledgements

The author wishes to thank Andrew Ross, Ralph Burton and Stephen Mobbs (University of Leeds) and Andy Brown and Roy Kershaw (Met Office) for helpful discussions held during the course of this work.

Appendix

The pressure-matching condition

The linear theory presented in section 5 is based on the shallow-convection form of the Boussinesq equations. In nonlinear form these can be written as

$$\frac{\mathrm{D}\mathbf{u}}{\mathrm{D}t} = -\nabla P' + \frac{g(\theta - \overline{\theta})}{\overline{\theta}_0}\mathbf{k}, \tag{A.1}$$

$$\frac{\mathrm{D}\theta}{\mathrm{D}t} = 0 \tag{A.2}$$

and

$$\nabla \cdot \mathbf{u} = 0, \tag{A.3}$$

where $\mathbf{u}$ is the velocity, θ is potential temperature, $P' = p'/\overline{\rho}_0$ and $\overline{\rho}_0$ is a constant reference density. The background (height dependent) potential temperature is represented by $\overline{\theta}$, and $\overline{\theta}_0$ is a constant reference value. We require that P' is continuous across the inversion and, following Baines (1995, p. 165), the matching conditions across the discontinuity can be obtained by expressing P' at $z' = 0$ as a Taylor series expansion about the displaced height of the inversion, $z' = \eta$:

$$P'_j(x, z' = 0) = P'(x, \eta) - \eta \frac{\partial P'_j}{\partial z}_{z'=\eta} + \mathrm{O}(\eta^2), \tag{A.4}$$

where the subscript j takes the values 1 or 2 and defines the layer beneath or above inversion, respectively. Since we require $P'_1 = P'_2$ at $z' = \eta$, Eq. (A.4) gives

$$(P'_1 - P'_2)_{z'=0} = \eta \left(\frac{\partial P'_2}{\partial z} - \frac{\partial P'_1}{\partial z} \right)_{z'=\eta}. \tag{A.5}$$

We may now use the vertical component of (A.1) to eliminate $\partial P_j'/\partial z$ from (A.5), and the continuity of the vertical velocity (and hence the continuity of $\mathrm{D}w_j/\mathrm{D}t$) at $z' = \eta$ to obtain the following matching condition:

$$(P_1' - P_2')_{z'=0} = \eta \frac{g\,(\theta_2 - \theta_1)_{z'=\eta}}{\overline{\theta}_0} = \eta g'. \tag{A.6}$$

We now assume wave-like solutions of the form (4) to the steady linearized versions of Eqs. (A.1) to (A.3). In the absence of background shear, the linearized continuity equation and the x-component of the linearized momentum equation can be combined to give

$$\overline{U}\frac{\mathrm{d}\widehat{w}}{\mathrm{d}z} = \mathrm{i}k\widehat{P}. \tag{A.7}$$

Substituting this into the Fourier transformed (A.6), and noting that $ik\overline{U}\widehat{\eta} = \widehat{w}$, then gives

$$\overline{U}\left(\frac{\mathrm{d}\widehat{w}_1}{\mathrm{d}z} - \frac{\mathrm{d}\widehat{w}_2}{\mathrm{d}z}\right) = \frac{\widehat{w}_1}{\overline{U}}g' \tag{A.8}$$

which is the second matching condition given in Eq. (9).

REFERENCES

Baines, P. G 1995 *Topographic effects in stratified flow*. Cambridge University Press

Belcher, S. E. and Wood, N. 1996 Form and wave drag due to stably stratified turbulent flow over low ridges. *Q. J. R. Meteorol. Soc.*, **122,** 863–902

Colman, B. R. and Dierking, C. F. 1992 The Taku wind of southeast Alaska: Its identification and prediction. *Weather and Forecasting*, **7,** 49–64

Dorman, C. E. and Winant, C. D. 1995 Buoy observations of the atmosphere along the west coast of the United States, 1981–1990. *J. Geophys. Res.*, **100,** C8, 16029–16044

Doyle, J. D. and Durran, D. R. 2002 The dynamics of mountain-wave-induced rotors. *J. Atmos. Sci.*, **59,** 186–201

Durran, D.R 1986 Another look at downslope windstorms. Part I: The development of analogs to supercritical flow in an infinitely deep, continuously stratified fluid. *J. Atmos. Sci.*, **43,** 2527–2543

1992 Two-layer solutions to Long's equation for vertically propagating mountain waves: How good is linear theory? *Q. J. R. Meteorol. Soc.*, **118,** 415–433

Durran, D. R. and Klemp, J. B. 1982 The effects of moisture on trapped mountain lee waves. *J. Atmos. Sci.*, **39,** 2490–2506

1983 A compressible model for the simulation of moist mountain waves. *Mon. Weather Rev.*, **111,** 2341–2361

Epifanio, C. C. and Durran, D. R. 2001 Three-dimensional effects in high-drag-state flows over long ridges. *J. Atmos. Sci.*, **58,** 1051–1065

Gal-Chen, T. and Somerville R. 1975 On the use of a coordinate transformation for the solution of the Navier–Stokes equations. *J. Comp. Phys.*, **17,** 209–228

Holmboe, J. and Klieforth, H. 1957 'Investigation of mountain lee waves and the air flow over the Sierra Nevada'. Final Report. Contract No. AF19(604)-728, University of California ADNo. 133606, Dept. of Meteorology, University of California, Los Angeles

Klemp, J. B. and Lilly, D. K. 1975 The dynamics of wave-induced downslope winds. *J. Atmos. Sci.*, **32,** 320–339

Kuettner, J. 1939 Zur entstehung der föhnwalle. *Beitr. Phys. Frei Atmos.,* **25,** 251–299

Leonard, B. P., MacVean, M. K. and Lock, A. P. 1993 'Positivity-preserving numerical schemes for multidimensional advection'. NASA Tech. Memo. 106055, ICOMP-93-05, National Aeronautics and Space Administration, Greenbelt MD, USA

Lin, Y. L. and Wang, T. A. 1996 Flow regimes and transient dynamics of two-dimensional stratified flow over an isolated mountain ridge. *J. Atmos. Sci.*, **53,** 139–158

Ozawa, H., Kumiko, G. A., Koyuru, I. and Iwanami, K. 1998 Cirriform rotor cloud observed on a Canadian arctic ice cap. *Mon. Weather Rev.*, **126,** 1741–1745

Piacsek, S. A. and Williams, G. P 1970 Conservation properties of convection difference schemes. *J. Comput. Phys.*, **6,** 392–405

Ralph F. M., Neiman, P. J., Keller, T. L., Levinson, D. and Fedor, L. 1997 Observations, simulations and analysis of nonstationary trapped lee waves. *J. Atmos. Sci.*, **54,** 1308–1333

Ross, A. N. and Vosper, S. B. 2003 Numerical simulations of stably stratified flow through a mountain pass. *Q. J. R. Meteorol. Soc.*, **129,** 97–115

Sawyer, J. S. 1960 Numerical calculation of the displacements of a stratified airstream crossing a ridge of small height. *Q. J. R. Meteorol. Soc.*, **86,** 326–345

Schär, C., and Durran, D. R 1997 Vortex formation and vortex shedding in continuously stratified flows past isolated topography. *J. Atmos. Sci.*, **54,** 534–554

Scorer, R. S. 1949 Theory of lee waves of mountains. *Q. J. R. Meteorol. Soc.*, **75,** 41–56.

Smith, R. B. 1976 The generation of lee waves by the Blue Ridge. *J. Atmos. Sci.*, **33,** 507–519

Smolarkiewicz, P. K., and Rotunno, R. 1989 Low Froude number flow past three-dimensional obstacles. Part I: Baroclinically generated lee vortices. *J. Atmos. Sci.*, **46,** 1154–1164

Ström, L., Tjernström, M. and Rogers, D. P. 2001 Observed dynamics of coastal flow at Cape Mendocino during Coastal Waves 1996. *J. Atmos. Sci.*, **58,** 953–977

Wang, T. A. and Lin, Y. L. 2000 Effects of shear and sharp gradients in static stability on two-dimensional flow over an isolated mountain ridge. *Meteorol. Atmos. Phys.*, **75,** 69–99

Wood, N. 1995 The onset of separation in neutral, turbulent flow over hills. *Boundary-Layer Meteorol.*, **76,** 137–164

Wood, N. and Mason, P. J. 1993 The pressure force induced by neutral, turbulent flow over hills. *Q. J. R. Meteorol. Soc.*, **119,** 1233–1267

Yang, T. S. and Akylas, T. R. 1996 Finite-amplitude effects on steady lee-wave patterns in subcritical stratified flow over topography. *J. Fluid Mech.*, **308,** 147–170